Nanocrystalline structure and microhardness of cobalt-chromium alloys electrochemically synthesized using a metal hydroxide coprecipitation technique

To cite this article: Ryusei Saeki and Takeshi Ohgai 2022 *Mater. Res. Express* **9** 026515

Materials Research Express

PAPER

Nanocrystalline structure and microhardness of cobalt-chromium alloys electrochemically synthesized using a metal hydroxide coprecipitation technique

Ryusei Saeki[1,*] **and Takeshi Ohgai**[2,*]

[1] Graduate School of Engineering, Nagasaki University, Bunkyo-machi 1-14, Nagasaki 852-8521, Japan
[2] Faculty of Engineering, Nagasaki University, Bunkyo-machi 1-14, Nagasaki 852-8521, Japan
[*] Authors to whom any correspondence should be addressed.

E-mail: bb52318101@ms.nagasaki-u.ac.jp **and** ohgai@nagasaki-u.ac.jp

Keywords: coprecipitation, electrodeposition, cobalt, chromium, nanocrystal, microhardness

OPEN ACCESS

RECEIVED
1 January 2022

REVISED
1 February 2022

ACCEPTED FOR PUBLICATION
7 February 2022

PUBLISHED
18 February 2022

Abstract

The effect of glycine as a complexing agent on metal hydroxide formation, such as $Co(OH)_2$ and $Cr(OH)_3$, was investigated based on potential-pH diagrams and titration curves for Co^{2+}-H_2O and Cr^{3+}—H_2O systems. Using a potentiostatic electrodeposition technique, Co–Cr alloy-based composite films containing Cr_2O_3 were synthesized from a non-suspended aqueous solution within an optimized pH range. Chromium content in the composite films was controlled up to 38.9% by adjusting the cathode potential during the alloy electrodeposition. Based on the XRD profiles and electron diffraction patterns, an amorphous-like nanocrystalline structure was observed in the composite films with high chromium content. The average crystal grain size declined due to Cr_2O_3 particles and hydrogen evolution during the electrodeposition process. Saturation magnetization of the composite films decreased with an increase in the chromium content. Synergistic contribution of increasing dislocation density and refining crystal grain size improved the microhardness of the composite films. The microhardness reached 624.2 kgf mm^{-2} and greatly exceeded that of pure cobalt (ca. 250–300 kgf mm^{-2}).

1. Introduction

Metal-based composite (MBC) films containing a certain amount of metal oxide fine particles (Cr_2O_3, Al_2O_3, SiO_2, TiO_2, etc) have attracted much attention due to their characteristic performance, such as mechanical, electromagnetic, and electrochemical properties. So far, various types of MBC films (e.g., Fe–Ni alloy with TiO_2 [1], Co metal with Cr_2O_3, Ni metal with Cr_2O_3 [2], Co–Ni alloy with Al_2O_3 [3]) have been synthesized using an electrodeposition technique. Some researchers have reported that the MBC films exhibited excellent mechanical properties and corrosion resistance. Xiong *et al* investigated the crystal structure and microhardness of electrodeposited CoNiP alloy-based composite films with Cr_2O_3 [4]. Their report revealed that the microhardness was improved by increasing the content of Cr_2O_3 particles in the electrodeposited alloy films. They concluded that the improvement of microhardness was caused by the crystal grain size refinement, which was induced by increasing the crystal nucleation density during the electrodeposition. Usually, MBC films can be synthesized by a co-electrodeposition of metals and particles using an electrolytic solution containing suspended fine particles [5]. However, there are some technical difficulties in the co-electrodeposition of metals and particles using a suspension type bath. In the co-electrodeposition of metals and particles, a vigorous stirring technique and controlling the concentration of the dispersing agent are required to prevent the agglomeration of fine particles during the electrodeposition. Furthermore, it is difficult to create a homogeneous dispersion of fine particles in the electrodeposited MBC films because fine particle agglomeration easily occurs on the cathode. However, recently, an electrodeposition method has been proposed to use a non-suspended bath to synthesize MBC films that include metal oxide or hydroxide nanoparticles [6]. During metal deposition from an

electrolytic solution, the pH near the cathode surface increases with increasing current density due to the reduction of hydrogen ions. Hayashi *et al* explored the fabrication process of MBC films via the hydrolysis reaction of metal ions [7]. Molybdenum oxide ions (MoO_4^{2-}) or tungsten oxide ions (WO_4^{2-}) can be reduced to the metallic state in the presence of iron-group metal ions (Ni^{2+}, Co^{2+}, Fe^{2+}, etc) [8, 9]. However, chromium ions (Cr^{3+}, etc) will transform to hydroxide or oxide through dehydration reaction near the cathode surface with increasing current density [10]. After the transformation, the chromium hydroxide is reduced to the metallic state.

Co–Cr alloys are widely used as biomaterials, such as artificial knee joints and dental prostheses, due to their excellent corrosion resistance and biocompatibility [11, 12]. Also, ferromagnetic Co–Cr alloys can be applied to high-density magnetic recording media [13, 14]. So far, an aqueous solution containing hexavalent chromium ions (Cr^{6+}) was used for electrodeposition of metallic chromium and its alloys. However, Cr^{6+} ions can harm the human body and induce environmental pollution [15, 16]. As an alternative to Cr^{6+} ions, trivalent chromium ions (Cr^{3+}) have been considered the most promising candidate to realize an environmental-friendly electrodeposition method of chromium alloys. Cr^{3+} ions can form complexes with six water molecules ($[Cr(H_2O)_6]^{3+}$). The $[Cr(H_2O)_6]^{3+}$ ions inhibit the electrochemical reduction process to the metallic state because the $[Cr(H_2O)_6]^{3+}$ ions can form a hydroxo-bridged colloidal polymer through the hydrolysis reaction in an acidic pH region ($pH > 4.5$) [17, 18]. Hence, an acidic bath ($pH < 2$) has been used so far for the electrodeposition of metallic chromium. However, pH in the vicinity of cathode will increase with a decrease in the concentration of proton (H^+) due to the hydrogen evolution during an electrolysis with a high current density. To avoid the hydrolysis reaction at the vicinity of cathode, complexing agents such as glycine, dimethylformamide (DMF), and formic acid should be added to the electrolysis bath because Cr^{3+} ions can form the stable complex ions with these complexing agents even in a neutral pH range. For example, Li *et al* investigated the Cr^{3+}-glycine complexes in an acidic aqueous solution by UV-visible spectrophotometry [19]. Based on their report, the formation of complex species such as $[Cr(gly)(H_2O)_4]^{2+}$ ions was promoted with an increase in the gly:Cr ratio ($1 < gly/Cr < 2.5$). Some researchers have reported that metallic chromium films were able to be electrodeposited from an aqueous solution containing the above complexing agents [20–22]. Among of them, glycine is an attractive complexing agent because it is harmless to the human body and global environment. The formation process of Cr^{3+}-glycine complexes and the electrochemical reduction process to the metallic state can be expressed by the following equations (1)–(3) [19, 23]

$$[Cr(H_2O)_6]^{3+} + \text{glycine} \rightarrow [Cr(gly)(H_2O)_4]^{2+} + 2H_2O \quad (1)$$

$$[Cr(gly)(H_2O)_4]^{2+} + e^- \rightarrow [Cr(gly)(H_2O)_4]^{+} \quad (2)$$

$$[Cr(gly)(H_2O)_4]^{+} + 2e^- \rightarrow Cr(metal) + 4H_2O + \text{glycine} \quad (3)$$

According to equation (1), with increasing the glycine concentration in the electrolytic solution, $[Cr(H_2O)_6]^{3+}$ ions will transform to $[Cr(gly)(H_2O)_4]^{2+}$ ions. Then, as shown in equation (2), $[Cr(gly)(H_2O)_4]^{2+}$ ions will be reduced on a cathode to $[Cr(gly)(H_2O)_4]^{+}$ ions which can act as an electroactive intermediate. Finally, the electroactive $[Cr(gly)(H_2O)_4]^{+}$ ions will be reduced to metallic chromium as shown in equation (3). According to the above complexing mechanism due to glycine, the olation reaction of $[Cr(H_2O)_6]^{3+}$ ions in the vicinity of cathode will be inhibited. Furthermore, the pH buffer activity of glycine will also be effective to inhibit the olation reaction [24]. Structure and corrosion resistance of the electrodeposited Co–Cr alloy films have been explored [25, 26]. In contrast, there are few reports on the mechanical properties of Co–Cr alloys that were electrochemically synthesized from an electrolytic solution containing Cr^{3+} ions. Mechanical properties such as tensile strength, ductility, and microhardness are important indexes to assess whether the materials can be applied to a practical application. Microstructures strongly affect the mechanical properties of electrodeposited films. Surface morphology, crystal grain size, and alloy composition of electrodeposited metallic films can be controlled by adjusting some electrolysis parameters, such as solution composition, temperature, pH, current density, cathode potential, etc. It is also possible to synthesize metal/ceramics composite films by utilizing an electrodeposition method with a large over potential.

Hence, in this study, the effects of the complexing agent (glycine) on the pH buffer activity of an electrolytic bath were examined to reveal the hydrolysis behavior of Co^{2+} and Cr^{3+} ions based on the potential-pH diagrams and titration curves. Then, Co–Cr alloy-based composite films containing Cr_2O_3 were synthesized by a potentiostatic electrodeposition technique from an aqueous chloride bath containing glycine. Furthermore, the effects of microstructure and chemical state of electrodeposited composite films on saturation magnetization and microhardness were also investigated.

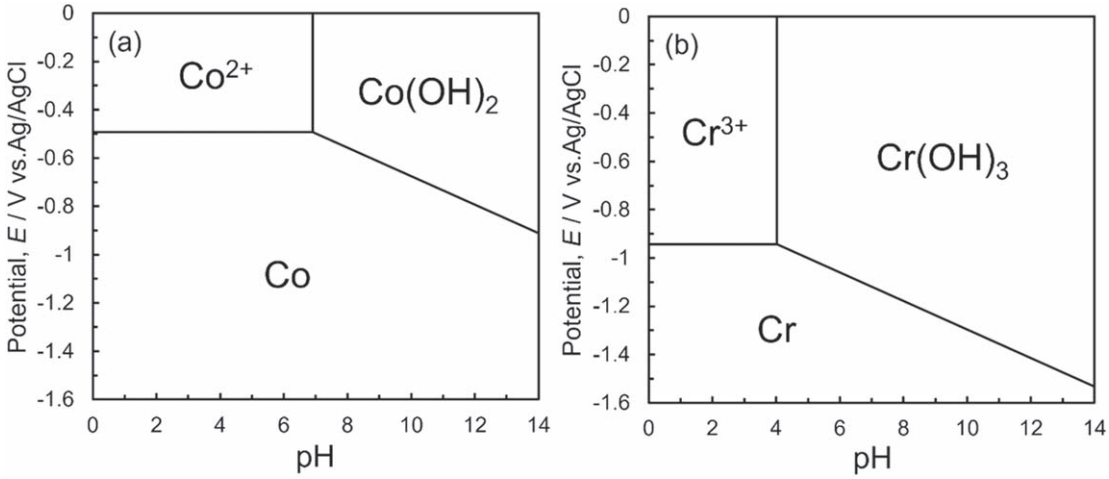

Figure 1. Potential-pH diagrams for Co^{2+}-H_2O (a) and Cr^{3+}-H_2O (b) systems at 25 °C.

2. Method

Co–Cr alloy-based composite films were synthesized by a potentiostatic electrodeposition technique using an electrolytic solution containing 0.25 M cobalt chloride hexahydrate, 0.5 M chromium chloride hexahydrate, 0.4 M boric acid, 1.0 M glycine, and 1.0 M ammonium chloride. The solution temperature and pH were adjusted to 40 °C and ca. 1.6, respectively, while the electrolytic bath was stirred using a magnetic stirrer (300 rpm) during the electrodeposition. A copper foil and a carbon rod were utilized as cathodes and anodes, respectively, while a silver chloride electrode (Ag/AgCl/Sat. KCl) was used as a reference electrode. Cathode potentials during the electrodeposition were fixed to −1.0 V, −1.5 V, −2.0 V, −2.5 V, −3.0 V, and −3.5 V versus Ag/AgCl, which were determined based on the cathodic polarization curve.

The alloy composition of electrodeposited Co–Cr alloy-based composite films was evaluated using Inductively Coupled Plasma Optical Emission Spectrometry (ICP-OES, ULTIMA2, Horiba Ltd, Kyoto, Japan). Surface texture of the electrodeposited alloy samples was investigated using Scanning Electron Microscopy (SEM, JCM-5700, JEOL Ltd, Tokyo, Japan). Constituent phases were identified using Transmission Electron Microscopy (TEM, JEM-2010-HT, JEOL Ltd, Tokyo, Japan) and an x-ray Diffractometer (XRD, Miniflex 600-DX, Rigaku Corp., Tokyo, Japan). Chemical state of cobalt and chromium in the electrodeposited films was analyzed using x-ray Photoelectron Spectroscopy (XPS, AXIS-ULTRA, Shimadzu Corp., Kyoto, Japan). Saturation magnetization of the electrodeposited films was investigated using a Vibrating Sample Magnetometer (VSM, TM-VSM1014-CRO, Tamakawa Co., Sendai, Japan) at room temperature. Microhardness of the electrodeposited films was measured using a micro-Vickers hardness testing machine (HM-211, Mitutoyo, Kanagawa, Japan). The microhardness test was performed on a polished cross-section of the electrodeposited films by applying a load of 0.05 kgf. For comparison, the saturation magnetization and microhardness of commercially available cobalt foil (NILACO, Co-103228, purity: 99.9%) were also investigated.

3. Results and discussion

3.1. Potential-pH diagrams for Co^{2+}-H_2O and Cr^{3+}-H_2O systems

Figure 1 shows the potential-pH diagrams for Co^{2+}-H_2O (a) and Cr^{3+}-H_2O (b) systems at 25 °C. Based on the potential-pH diagrams, the thermodynamically stable state of chemical species can be estimated. These diagrams were plotted using the standard electrode potentials of Co/Co^{2+} and Cr/Cr^{3+} ($E_{Co}^{\circ} = -0.474$ V, $E_{Cr}^{\circ} = -0.937$ V versus Ag/AgCl), the stability constants of $Co(OH)_2$ and $Cr(OH)_3$ ($pK_{sp} = 14.8, 30.2$ [27]), and Nernst's equation. According to figure 1(a), it is predicted that the electrodeposition of metallic cobalt will be possible at the cathode potential region less-noble than the equilibrium potential of Co/Co^{2+} ($E_{Co}^{eq} = -0.492$ V versus Ag/AgCl). In addition, Co^{2+} ions can form hydroxide when the solution pH increases up to 6.9. Conversely, the electrodeposition of metallic chromium will be possible at the cathode potential region less-noble than the equilibrium potential of Cr/Cr^{3+} ($E_{Cr}^{eq} = -0.943$ V versus Ag/AgCl) according to the potential-pH diagram for the Cr^{3+}-H_2O system (figure 1(b)). Furthermore, it is also predicted that Cr^{3+} ions can form hydroxide when the solution pH rises to 4.0. During the electrodeposition process from an aqueous solution, pH in the vicinity of cathode increases with decreasing H^+ ions concentration due to the hydrogen evolution at a

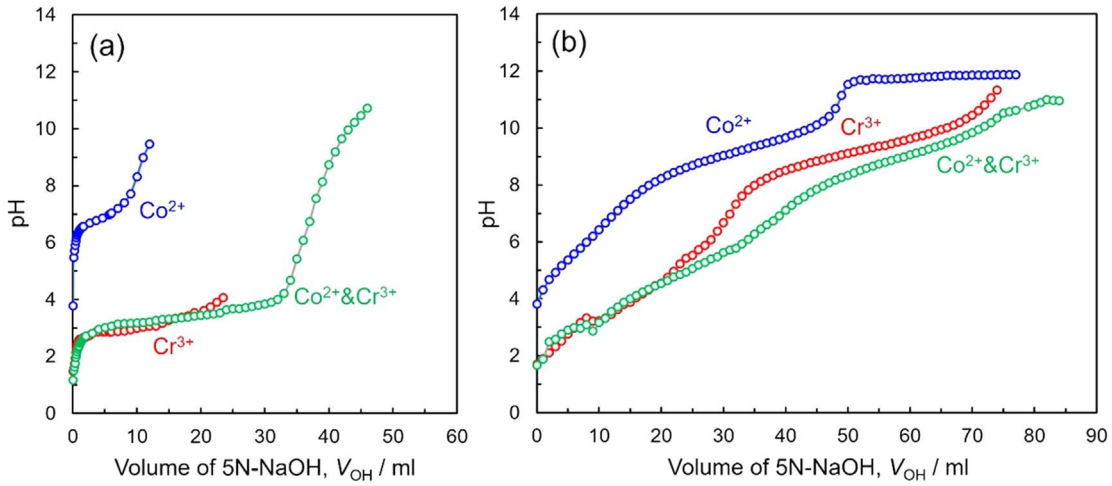

Figure 2. Titration curves for aqueous solutions A, B, and C without glycine (a). Titration curves for aqueous solutions D, E, and F with glycine (b). Solution A and D (in blue lines) contain Co^{2+} ions (0.25 M). Solution B and E (in red lines) contain Cr^{3+} ions (0.5 M). Solution C and F (in green lines) contains Co^{2+} ions (0.25 M) and Cr^{3+} ions (0.5 M). These solutions contain boric acid (0.4 M) as an additive and each solution was kept to 40 °C.

high current density. Therefore, it seems to be quite difficult to make an electrochemical reduction of Cr^{3+} ions from an aqueous solution that does not contain complexing agents.

3.2. Titration curves of electrolytic solutions containing glycine

Figure 2(a) shows the titration curves for electrolytic solutions A, B, and C without glycine (solution A: $[Co^{2+}] = 0.25$ M, solution B: $[Cr^{3+}] = 0.5$ M, solution C: $[Co^{2+}] = 0.25$ M and $[Cr^{3+}] = 0.5$ M). These solutions contained 0.4 M boric acid as an additive, and each solution was kept to 40 °C. 5 M sodium hydroxide solution was dropped into these solutions during the titration. In solutions A and B, each pH was stabilized at 7 and 3, respectively. These pH buffer activities seem to be induced by the hydroxide formation process of Co^{2+} and Cr^{3+} ions because the pH7 and pH3 correspond well with the pH values that are estimated from the pH-potential diagrams for Co^{2+}-H_2O and Cr^{3+}-H_2O systems (figure 1). However, in solution C, the pH stabilized only at 3. Hence, Co^{2+} and Cr^{3+} ions seem to form hydroxides simultaneously at pH3. Such a phenomenon is known as 'coprecipitation'. The following several theories (I–III) have been proposed as the mechanism of coprecipitation [28, 29].

(I) **Substitution:** If the two kinds of heterologous metal ions have a similar size, the substitution of metal ions will occur at a lattice position of a metal hydroxide precipitate.

(II) **Occlusion:** Metal ions and solvent molecules will be trapped in the metal hydroxide precipitate.

(III) **Adsorption:** Metal and hydroxide ions will be adsorbed on the surface of the metal hydroxide precipitate.

Cr^{3+} ions seem to exist as $Cr_2O_3 \cdot nH_2O$ or $Cr(OH)_3$ in the hydroxide precipitate. Cr_2O_3 and $Co(OH)_2$ have the same hexagonal structure. Furthermore, the ionic radii of Cr^{3+} (61.5 pm [30]) and Co^{2+} (65 pm [30]) are quite similar in value. Hence, the mixed crystal of Cr_2O_3 and $Co(OH)_2$ will be formed due to the above-mentioned coprecipitation process.

Figure 2(b) shows the titration curves for electrolytic solutions D, E, and F (40 °C) containing glycine (solution D: $[Co^{2+}] = 0.25$ M, solution E: $[Cr^{3+}] = 0.5$ M, solution F: $[Co^{2+}] = 0.25$ M and $[Cr^{3+}] = 0.5$ M). These solutions contained 0.4 M boric acid and 1.0 M ammonium chloride. Similarly, 5 M sodium hydroxide solution was used for the titrations. These solutions showed pH buffer activities around pH 9. In solutions D, E, and F with glycine, no clear stagnation of pH value was observed, unlike the pH buffer activities of solutions A, B, and C without glycine. Hence, the effect of glycine addition seems to suppress the formation of chromium hydroxide in the low pH region (~pH 4) and the production of cobalt hydroxide associated with the coprecipitation phenomenon.

3.3. Electrodeposition of Co–Cr alloy-based composite films

To investigate the electrodeposition behavior of Co–Cr alloy-based composite films, a cathodic polarization curve was plotted (figure 3(a)). During the measurement, the bath temperature was kept at 40 °C, and the potential was scanned at a rate of 50 mVs^{-1}. The bath composition and electrodes were the same as those used for electrodepositing the composite films. From figure 3(a), by scanning the electrode potential to a less-noble

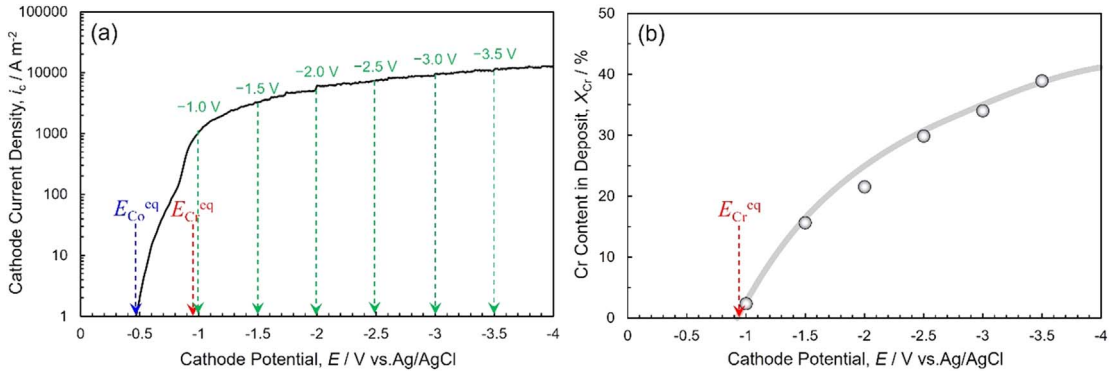

Figure 3. Cathodic polarization curve during the electrodeposition of Co-Cr alloy-based composite films (a). The bath temperature was kept to 40 °C, and the potential scan rate was set to 50 mVs^{-1}. Effect of cathode potential on the chromium content (X_{Cr}) in Co-Cr alloy-based composite films (b).

region, the cathode current density began to increase sharply at the electrode potential of ca. −0.5 V versus Ag/AgCl. According to Nernst's equation, the equilibrium potential of Co/Co^{2+} (E_{Co}^{eq}) can be calculated to ca. −0.49 V versus Ag/AgCl based on the bath temperature and metal ions concentration (40 °C, [Co^{2+}] = 0.25 M). Hence, the increase in the cathode current density should be caused by the deposition current of Co^{2+} ions. Subsequently, by scanning the electrode potential to a less-noble region, the cathode current density significantly increased again at the electrode potential region of ca. −0.85 V versus Ag/AgCl. Likewise, the equilibrium potential of Cr/Cr^{3+} (E_{Cr}^{eq}) can be determined to ca. −0.94 V versus Ag/AgCl ([Cr^{3+}] = 0.5 M). Hence, it is considered that the deposition of metallic chromium began to proceed at a potential region which is nobler than the theorical equilibrium potential due to an under potential deposition (UPD) phenomenon. Although the mechanism of UPD remains unsolved, some researchers have proposed that some kinds of metal ions (Cd^{2+}, Zn^{2+}, etc) can be deposited by a way of the hydroxide intermediates, even in a potential region that is nobler than the equilibrium potential [31]. Furthermore, by shifting the potential to a region that is less noble than −1.0 V versus Ag/AgCl, the slope of the polarization curve decreased due to the decrease in H$^+$, Co^{2+}, and Cr^{3+} ion concentrations in the vicinity of cathode. Consequently, for electrodepositing Co–Cr alloy-based composite films, the optimum cathode potential condition was determined, ranging from −1.0 V to −3.5 V versus Ag/AgCl.

Figure 3(b) shows the effect of cathode potential on the chromium content (X_{Cr}) in Co–Cr alloy-based composite films. By scanning the electrode potential to a less-noble region, X_{Cr} in the alloy films increased. According to figures 3(a) and (b), the co-deposition behavior of Co–Cr alloys in this study can be considered a 'normal co-deposition type' based on Brenner's classification [32]. In the normal co-deposition type, the metal ions, which have an electrochemically nobler equilibrium potential (i.e., cobalt), were preferentially deposited rather than the less-noble metal ions (i.e., chromium). In this study, X_{Cr} in Co–Cr alloy-based composite films increased up to 38.9% by scanning the electrode potential down to −3.5 V versus Ag/AgCl.

3.4. Structure of electrodeposited Co–Cr alloy-based composite films

Figure 4 shows the effect of chromium content on the SEM images of Co–Cr alloy-based composite films ((a) X_{Cr} = 2.4%, (b) X_{Cr} = 15.6%, (c) X_{Cr} = 21.5%, (d) X_{Cr} = 29.9%, (e) X_{Cr} = 34.0%, (f) X_{Cr} = 38.9%). From figure 4(a) in the sample with X_{Cr} of 2.4%, a needle-shaped microstructure was observed. In contrast, from figures 4(b)–(f), by increasing X_{Cr} from 15.6% to 38.9%, a nodule-like morphology was confirmed. Especially, from figures 4(e) and (f), the samples with high chromium content (X_{Cr} = 34.0% and 38.9%) had some microcracks, which seem to be caused by hydrogen embrittlement. As shown in figure 3(b), with increasing the cathode potential, the chromium content also increased. It is well known that the crystal nucleation density of electrodeposited metals increases with an increase in the cathodic overpotential if the rate-determining process is the charge transfer on the electrode [33]. According to figure 3(a), at the cathode potential region nobler than −1.1 V, the charge transfer process seems to be the rate-determining. Hence, the sample (figure 4(a)) which was obtained at −1.0 V seems to be composed of fine grains with relatively smooth surface due to the uniform nucleation. On the other hand, the reduction rate seems to be controlled by the mass transfer process of metal ions in the potential region less noble than −1.1 V. In this potential region, the sub-reaction such as hydrogen evolution will proceed on the cathode and the non-uniform nucleation process will be occurred during the electrodeposition process. Consequently, the nodule-like deposits seem to be caused on the surface of electrodeposited films with high chromium content (figures 4(b)–(f)).

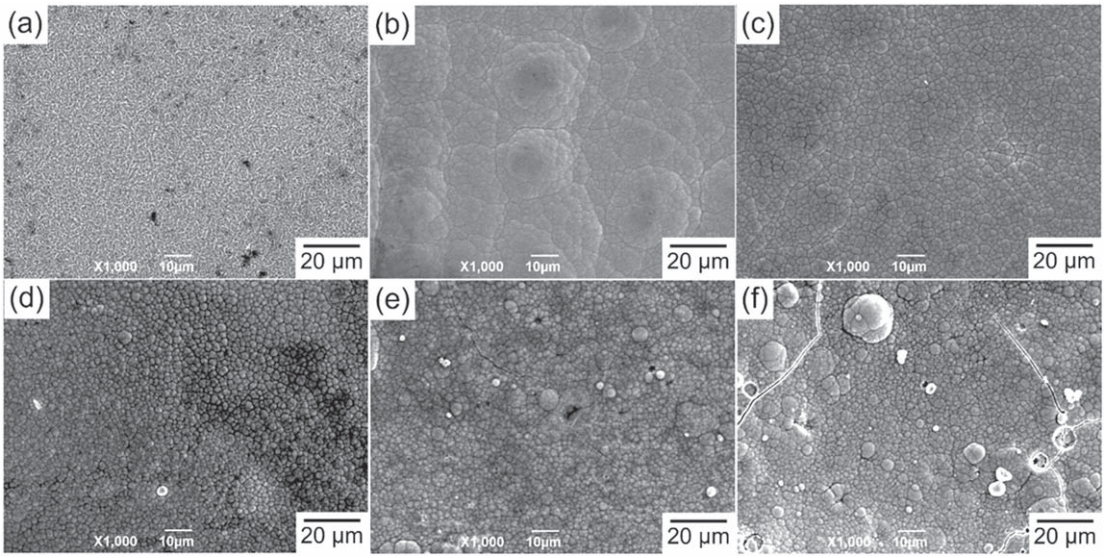

Figure 4. Effect of chromium content on the SEM images of Co-Cr alloy-based composite films ((a) $X_{Cr} = 2.4\%$, (b) $X_{Cr} = 15.6\%$, (c) $X_{Cr} = 21.5\%$, (d) $X_{Cr} = 29.9\%$, (e) $X_{Cr} = 34.0\%$, (f) $X_{Cr} = 38.9\%$).

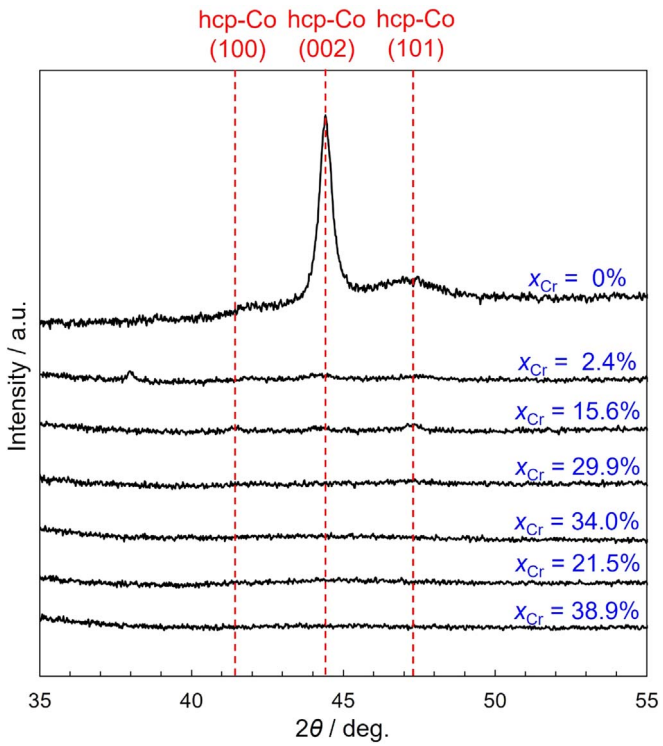

Figure 5. Effect of chromium content on the XRD profiles of pure Co and Co-Cr alloy-based composite films that were separated from copper substrates.

The increase in X_{Cr} will cause the disturbance of the atomic arrangement in the cobalt crystal lattice. Figure 5 shows the effect of chromium content on the XRD profiles of Co–Cr alloy-based composite films that were separated from copper substrates. For comparison, the XRD profile of pure Co film ($X_{Cr} = 0\%$) was added in figure 5. The Co film was electrochemically synthesized from an aqueous solution (40 °C) containing 1.0 M cobalt sulfate and 0.4 M boric acid. In the profile of electrodeposited Co film, the sharp peak associated with hcp-Co (0 0 2) was observed. In addition, the small peaks associated with hcp-Co (1 0 0) and (1 0 1) were also confirmed. Based on the XRD profile, the electrodeposited Co film seems to have a crystalline structure. On the contrary, in the composite films with X_{Cr} of 2.4% and 15.6%, broad peaks associated with hcp-Co (1 0 0), (0 0 2), and (1 0 1) were observed. However, in the composite films with X_{Cr} exceeding 20%, no diffraction peaks were

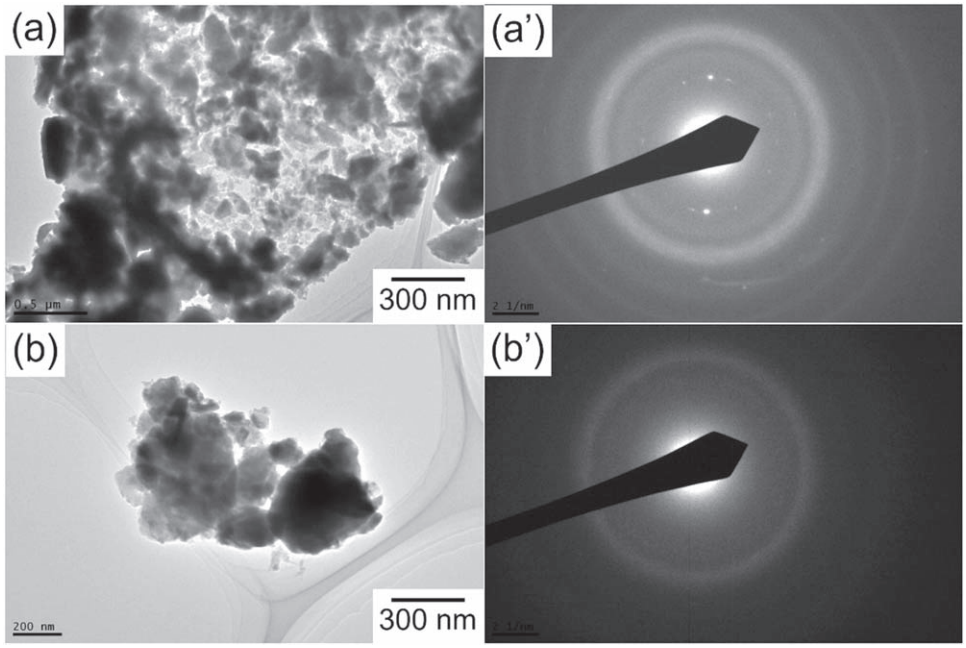

Figure 6. Effect of chromium content on the TEM bright field images (a) and (b) and electron diffraction patterns (a′) and (b′) of Co-Cr alloy-based composites ((a) $X_{Cr} = 15.6\%$ and (b) $X_{Cr} = 34.0\%$).

confirmed. Figure 6 shows the effect of chromium content on the TEM bright field images ((a) and (b)) and electron diffraction patterns ((a′) and (b′)) of Co–Cr alloy-based composites ((a) $X_{Cr} = 15.6\%$ and (b) $X_{Cr} = 34.0\%$). From figures 6(a)′ and (b)′, concentric and vague diffraction patterns (halo-patterns) were observed. Hence, figures 5 and 6 show that the structure of Co–Cr alloy-based composite films was transformed from a nanocrystalline phase to an amorphous phase with an increase in X_{Cr}.

The chemical binding energy of cobalt (figure 7) and chromium (figure 8) in Co–Cr alloy-based composite films was investigated according to the XPS spectra. The surface of each sample was etched by argon ions for a duration of 0, 12, 24, 36, 48 and 60 min. Based on a reference [34], the binding energy derived from metallic cobalt corresponds to 792.95 eV ($Co^{\circ}-2p_{1/2}$) and 777.9 eV ($Co^{\circ}-2p_{3/2}$). Notably, iron-group metal ions ($M^{2+} = Fe^{2+}, Co^{2+}, Ni^{2+}$) can form hydroxide ions ($M(OH)^{+}$), and the ions can adsorb on the surface of cathode [35]. Subsequently, the $M(OH)^{+}$ ions will be reduced to the metallic state as electrodeposited crystals via a multi-step reaction process. Therefore, cobalt seems to exist as a metallic state in Co–Cr alloy-based composite films. However, the binding energy derived from metallic chromium corresponds to 583.4 eV ($Cr^{\circ}-2p_{1/2}$) and 574.1eV ($Cr^{\circ}-2p_{3/2}$), while that of trivalent chromium corresponds to 586.3 eV ($Cr^{3+}-2p_{1/2}$) and 576.6eV ($Cr^{3+}-2p_{3/2}$) [36]. Hence, according to the XPS spectra (figure 8), chromium seems to exist as a mixture of metallic and oxide states. Based on the above experimental results, chromium ions should form hydroxide in the vicinity of the cathode through a hydrolysis reaction during the electrodeposition process with a large over potential. Furthermore, the hydroxide could form metallic oxide and be included into the electrodeposited alloy film via dehydration reaction. Figure 9 shows the electrodeposition mechanism of Co-Cr alloy-based composite films by way of the glycine complex precursors. As mensioned above, an amorphous-like nanocrystalline structure was confilmed in the composite films. The crystal grain size seems to decline due to solute Cr atoms, Cr_2O_3 particles and hydrogen evolution during the electrodeposition process.

3.5. Magnetic and mechanical properties of Co–Cr alloy-based composite films

Figure 10 shows the effect of chromium content on the magnetic hysteresis loops of Co–Cr alloy-based composite films ((a) $X_{Cr} = 2.4\%$, (b) $X_{Cr} = 15.6\%$, (c) $X_{Cr} = 21.5\%$, (d) $X_{Cr} = 29.9\%$, (e) $X_{Cr} = 34.0\%$, (f) $X_{Cr} = 38.9\%$). An external magnetic field was applied to the in-plane direction of the electrodeposited alloy films during the magnetization measurement. Figure 11(a) shows the effect of chromium content on the saturation magnetization of Co–Cr alloy-based composite films. In the figure, the saturation magnetization value (146.3 emu g^{-1}) of commercially available pure cobalt foil (purity: 99.9%) was also plotted as $X_{Cr} = 0\%$. The saturation magnetization of Co–Cr alloy-based composite films decreased to zero with an increase in X_{Cr} up to ca. 40%. Ishida *et al* reported that the Curie temperature of Co–Cr alloys decreased to room temperature with an increase in X_{Cr} up to ca. 20% [37]. Hence, in this study, almost half of the Cr atoms seem to exist outside of the Co–Cr alloy phase. Figure 11(b) shows the effect of chromium content on the microhardness of Co–Cr alloy-

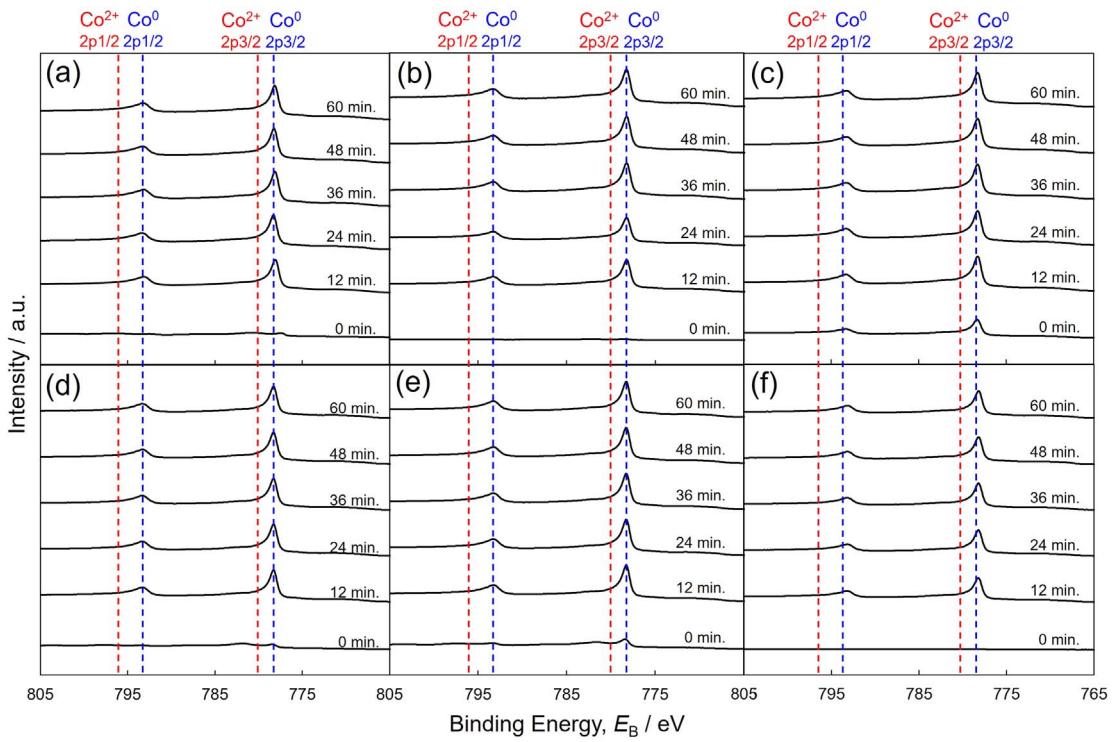

Figure 7. Effect of chromium content on the XPS spectra of Co binding energy region in Co-Cr alloy-based composite films ((a) $X_{Cr} = 2.4\%$, (b) $X_{Cr} = 15.6\%$, (c) $X_{Cr} = 21.5\%$, (d) $X_{Cr} = 29.9\%$, (e) $X_{Cr} = 34.0\%$, (f) $X_{Cr} = 38.9\%$). Surface of each sample was etched by argon ions for the duration of 0, 12, 24, 36, 48 and 60 min.

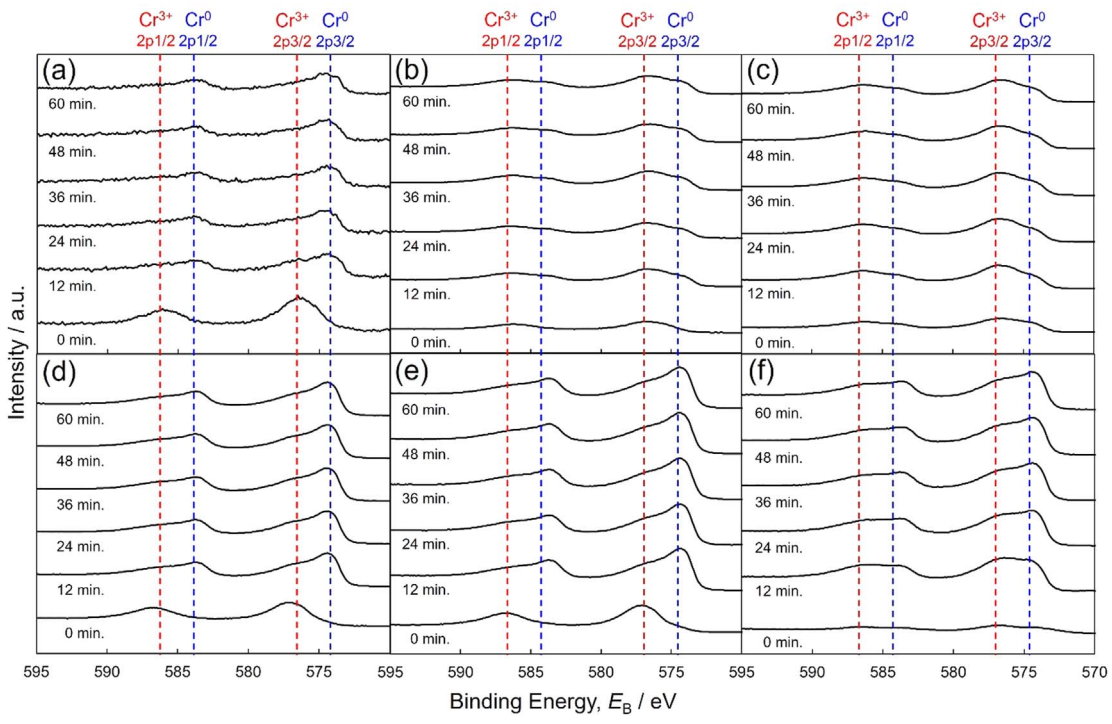

Figure 8. Effect of chromium content on the XPS spectra of Cr binding energy region in Co-Cr alloy-based composite films ((a) $X_{Cr} = 2.4\%$, (b) $X_{Cr} = 15.6\%$, (c) $X_{Cr} = 21.5\%$, (d) $X_{Cr} = 29.9\%$, (e) $X_{Cr} = 34.0\%$, (f) $X_{Cr} = 38.9\%$). Surface of each sample was etched by argon ions for the duration of 0, 12, 24, 36, 48 and 60 min.

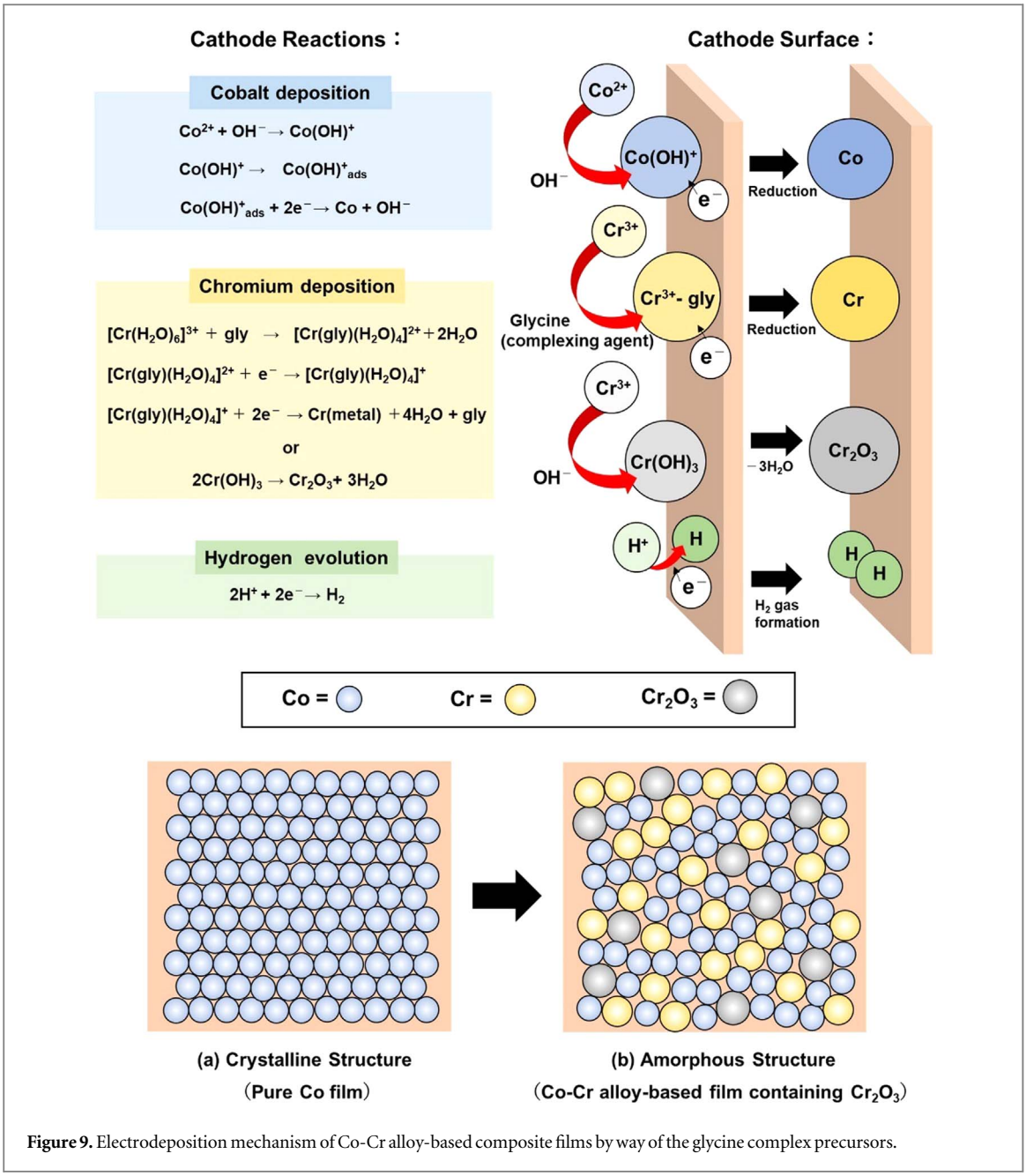

Figure 9. Electrodeposition mechanism of Co-Cr alloy-based composite films by way of the glycine complex precursors.

based composite films. It has been reported that the hardness of pure cobalt is approximately 250 to 300 kgf mm^{-2} ($HV_{0.05}$) [38, 39]. In this study, the microhardness of commercially available cobalt foil was determined to be 291.1 kgf mm^{-2} ($HV_{0.05}$). From figure 11(b), the microhardness increased up to 624.2 kgf mm^{-2} ($HV_{0.05}$) with an increase in X_{Cr} up to ca. 40%. According to the mechanism of solid solution strengthening of metallic materials, the density of lattice defects, such as dislocations and grain boundaries, increases with an increase in the concentration of solute atoms. Furthermore, the average crystal grain size will decrease with an increase in the density of lattice defects. Hence, in this study, the synergistic effect of solid solution strengthening and crystal grain refinement strengthening seems to have contributed to improving the microhardness of Co–Cr alloy-based composite films.

4. Conclusion

Based on the potential-pH diagrams and titration curves for Co^{2+}-H_2O and Cr^{3+}-H_2O systems, it was revealed that glycine as a complexing agent suppressed the formation of chromium hydroxide in the low pH region (~ pH 4) and the production of cobalt hydroxide associated with the coprecipitation phenomenon. Co–Cr alloy-based composite films containing Cr_2O_3 were synthesized from a non-suspended aqueous solution using a potentiostatic electrodeposition technique. Chromium content in the composite films was controlled up to

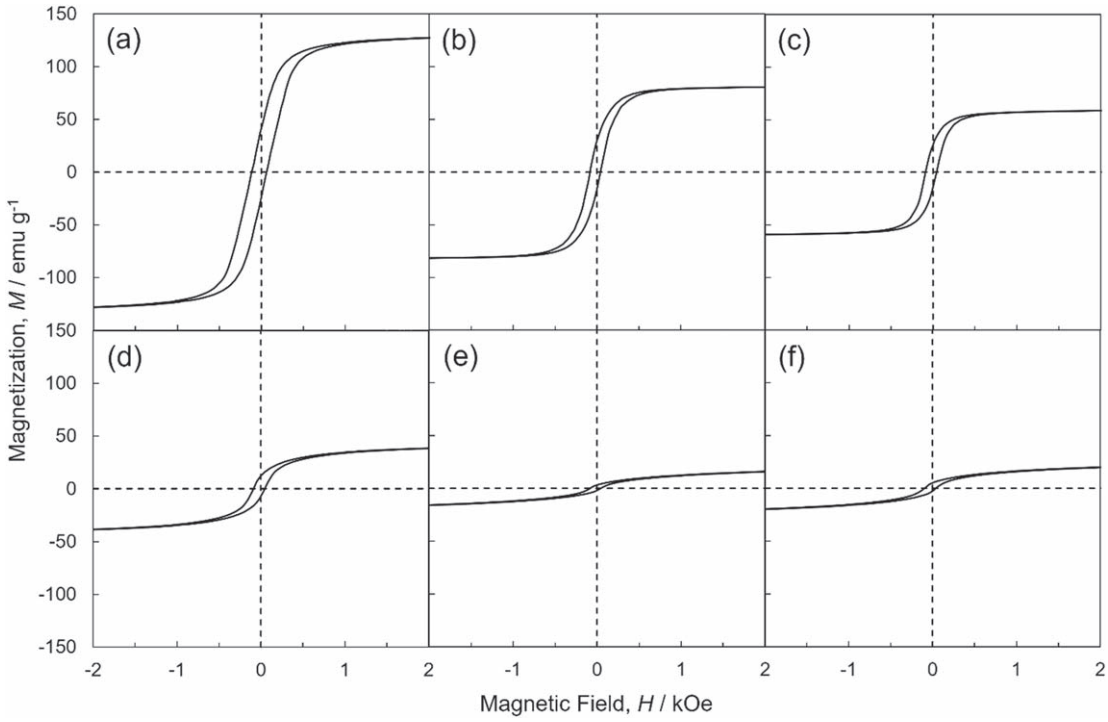

Figure 10. Effect of chromium content on the magnetic hysteresis loops of Co-Cr alloy-based composite films ((a) $X_{Cr} = 2.4\%$, (b) $X_{Cr} = 15.6\%$, (c) $X_{Cr} = 21.5\%$, (d) $X_{Cr} = 29.9\%$, (e) $X_{Cr} = 34.0\%$, (f) $X_{Cr} = 38.9\%$). An external magnetic field was applied to in-plane direction to the electrodeposited alloy films.

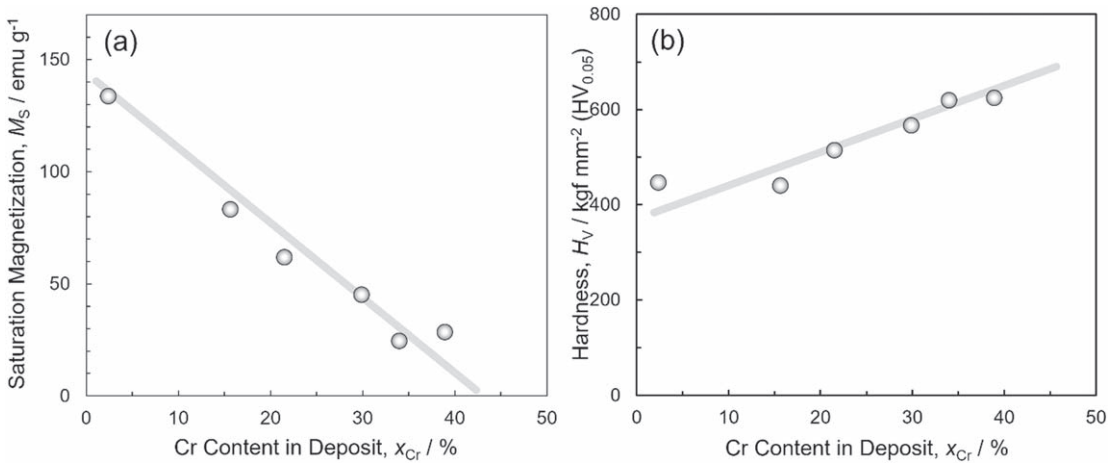

Figure 11. Effect of chromium content on the saturation magnetization (a) and microhardness (b) of Co-Cr alloy-based composite films.

38.9% by scanning the electrode potential down to −3.5 V versus Ag/AgCl. Amorphous-like nanocrystalline structure was observed in Co–Cr alloy-based composite films with high chromium content. Saturation magnetization of Co–Cr alloy-based composite films decreased to zero with an increase in X_{Cr} up to ca. 40%. Microhardness increased up to 624.2 kgf mm^{-2} with an increase in X_{Cr} up to ca. 40%. It was concluded that the synergistic effect of solid solution strengthening and crystal grain refinement strengthening contributed to improving the microhardness of Co–Cr alloy-based composite films.

Acknowledgments

The authors thank Japan Society for the Promotion of Science (JSPS: 18H01754 and 20J21925) for the financial support.

Data availability statement

The data that support the findings of this study are available upon reasonable request from the authors.

Declarations

Competing interests

The authors declare that they have no competing interests.

Authors' contributions

R S carried out experiments, analyzed data, and wrote manuscript. T O designed the study, supervised the project, and analyzed data. All authors read and approved the final manuscript.

ORCID iDs

Takeshi Ohgai https://orcid.org/0000-0001-6872-7888

References

[1] Yousefi E, Sharafi S and Irannejad A 2018 The structural, magnetic, and tribological properties of nanocrystalline Fe–Ni permalloy and Fe–Ni–TiO_2 composite coatings produced by pulse electro co-deposition *J. Alloys Compd.* **753** 308–19
[2] Kumar K, Chandramohan R and Kalyanaraman D 2004 Effect of heat treatment on cobalt and nickel electroplated surfaces with Cr_2O_3 dispersions *Appl. Surf. Sci.* **227** 383–6
[3] Wu G, Li N, Zhou D and Mitsuo K 2004 Electrodeposited Co–Ni–Al_2O_3 composite coatings. *Surf. Coat. Technol.* **176** 157–64
[4] Xiong W, Ma M, Zhang J and Lian Y 2020 The effects of Cr_2O_3 particles on the microstructure and wear-resistant properties of electrodeposited CoNiP coatings. *Surf. Coat. Technol.* **381** 125167
[5] Mbugua N S, Kang M, Zhang Y, Ndiithi N J, Bertrand G V and Yao L 2020 Electrochemical deposition of Ni, NiCo alloy and NiCo–ceramic composite coatings—a critical review *Materials* **13** 3475
[6] Nakano H, Ohgai T, Fukushima H, Akiyama T and Kammel R 2001 Factors determining the critical current density for zinc deposition in sulfate solutions *Metall* **55** 676–81
[7] Hayashi H 2006 Composite plating—codeposition mechanism and new application *J. Surf. Finish. Soc. Jpn.* **57** 466–70
[8] Ohgai T, Washio R and Tanaka Y 2012 Anisotropic magnetization behavior of electrodeposited nanocrystalline Ni–Mo alloy thin films and nanowires array *J. Electrochem. Soc.* **159** H800–4
[9] Ohgai T, Fujimaru T and Tanaka Y 2014 Isotropic magnetization response of electrodeposited nanocrystalline Ni–W alloy nanowire arrays *J. Appl. Electrochem.* **44** 301–7
[10] Akiyama T, Kobayashi S, Ki J, Ohgai T and Fukushima H 2000 Role of polyethylene glycol in electrodeposition of zinc–chromium alloys *J. Appl. Electrochem.* **30** 817–22
[11] Saravanan G and Mohan S 2012 Structure, composition and corrosion resistance studies of Co–Cr alloy electrodeposited from deep eutectic solvent (DES) *J. Alloys Compd.* **522** 162–6
[12] Baba N, Watanabe I, Liu J and Atsuta M 2004 Mechanical strength of laser-welded cobalt–chromium alloy *J. Biomed. Mater. Res. B Appl. Biomater.* **69** 121–4
[13] Chaure N B and Coey J M D 2006 Fabrication and characterization of electrodeposited $Co_{1-x}Cr_x$ nanowires *J. Magn. Magn. Mater.* **303** 232–6
[14] Najafi M, Alemipour Z, Hasanzadeh I, Aftabi A and Soltanian S 2015 Influence of annealing temperature, electrolyte concentration and electrodeposition conditions on magnetic properties of electrodeposited Co-Cr alloy nanowires. *J. Supercond. Nov. Magn.* **28** 95–101
[15] Mahdavi S and Allahkaram S R 2015 Composition, characteristics and tribological behavior of Cr, Co–Cr and Co–Cr/TiO_2 nano-composite coatings electrodeposited from trivalent chromium based baths *J. Alloys Compd.* **635** 150–7
[16] Ferreira E S C, Pereira C M and Silva A F 2013 Electrochemical studies of metallic chromium electrodeposition from a Cr(III) bath *J. Electroanal. Chem.* **707** 52–8
[17] Giovanardi R and Orlando G 2011 Chromium electrodeposition from Cr(III) aqueous solutions *Surf. Coat. Technol.* **205** 3947–55
[18] Saravanan G and Mohan S 2009 Corrosion behavior of Cr electrodeposited from Cr(VI) and Cr(III)-baths using direct (DCD) and pulse electrodeposition (PED) techniques *Corros. Sci.* **51** 197–202
[19] Wang F, Itoh K and Watanabe T 2002 Relationship between the crystallographic structure of electrodeposited Fe–Cr alloy film and its thermal equilibrium diagram *Mater. Trans.* **43** 439–42
[20] Wang F and Watanabe T 2003 Preparation and characterization of the electrodeposited Fe-Cr alloy film *Mater. Sci. Eng. A* **349** 183–90
[21] Saravanan G and Mohan S 2010 Structure, current efficiency, and corrosion properties of brush electrodeposited (BED) Cr from Cr(III) dimethyl formamide (DMF)-bath *J. Appl. Electrochem.* **40** 1–6
[22] Li B, Lin A, Wu X, Zhang Y and Gan F 2008 *J. Alloy. Compd.* **453** 93–101
[23] Lui S, Shohji I, Kobayashi T, Hirohashi J, Wake T, Yamamoto H and Kamakoshi, Y 2021 *J. Electroanal. Chem.* **897** 115582
[24] Bertero E, Manzano C V, Pellicer E, Sort J, Ulfig R M, Mischler S, Michler J and Philippe L 2019 *RSC Adv.* **9** 25762
[25] Survilienė S, Jasulaitienė V, Češūnienė A and Lisowska-Oleksiak A 2008 The use of XPS for study of the surface layers of Cr–Co alloy electrodeposited from Cr(III) formate–urea baths *Solid State Ion.* **179** 222–7

[26] Ohgai T, Tanaka Y and Fujimaru T 2012 Soft magnetic properties of Ni–Cr and Co–Cr alloy thin films electrodeposited from aqueous solutions containing trivalent chromium ions and glycine *J. Appl. Electrochem.* **42** 893–9
[27] Blais J F, Djedidi Z, Cheikh R B, Tyagi R D and Mercier G 2008 Metals precipitation from effluents: review *Practice Periodical of Hazardous, Toxic, and Radioactive waste Management (ASCE)* **12** 135–49
[28] Terada K 2000 Trace elements by coprecipitation: extraction *Encyclopedia of Separation Science (Academic)* 4394–402
[29] Yakushev A 2021 Probing precipitation properties *Nat. Chem.* **13** 213–5
[30] Shannon R D and Effective R 1976 Ionic radii and systematic studies of interatomie distances in halides and chaleogenides *Acta Cryst.* **A32** 751–67
[31] Ohgai T, Gravier L, Hoffer X and Ansermet J-P 2005 CdTe semiconductor nanowires and NiFe ferro-magnetic metal nanowires electrodeposited into cylindrical nano-pores on the surface of anodized aluminum *J. Appl. Electrochem.* **35** 479–85
[32] Zangari G 2015 Electrodeposition of alloys and compounds in the era of microelectronics and energy conversion technology *Coatings* **5** 195–218
[33] Saeki R and Ohgai T 2019 Determination of crystal growth geometry factors and nucleation site densities of electrodeposited ferromagnetic cobalt nanowire arrays *Crystals* **9** 142
[34] Ivill M, Pearton S J, Rawal S, Leu L, Sadik P, Das R, Hebard A F, Chisholm M, Budai J D and Norton D P 2008 Structure and magnetism of cobalt-doped ZnO thin films *New J. Phys.* **10** 065002
[35] Bockris J O ' M and Kita H 1961 Analysis of galvanostatic transients and application to the iron electrode reaction *J. Electrochem. Soc.* **108** 676–81
[36] Biesinger M C, Payne B P, Grosvenor A P, Lau L W M, Gerson A R and Smart R S C 2011 Resolving surface chemical states in XPS analysis of first row transition metals, oxides and hydroxides: Cr, Mn, Fe, Co and Ni *Appl. Surf. Sci.* **257** 2717–30
[37] Ishida K and Nishizawa T 1990 The Co-Cr (Cobalt-Chromium) system *Bulletin of Alloy Phase Diagrams* **11** 357–70
[38] Wang W, Hou Z, Raquel Lizárraga, Ye Tian, Babu R P, Holmström E, Mao H and Larsson H 2019 An experimental and theoretical study of duplex fcc+hcp cobalt based entropic alloys *Acta Mater.* **176** 11–8
[39] Simionescu N, Benea L and Celis J P 2019 Wear-corrosion response of Cerium oxide reinforced Cobalt hybrid composite layers in biological solution. *IOP Conf. Series: Materials Science and Engineering,* **572** 012003